ZAMM · Z. Angew. Math. Mech. **83**, No. 3, 181 – 196 (2003) / **DOI** 10.1002/zamm.200310018

Moderate-to-large injection and suction driven channel flows with expanding or contracting walls

J. Majdalani* **and C. Zhou**

Marquette University, Milwaukee, WI 53233, USA

Received 25 October 2000, revised 12 December 2001, accepted 9 April 2002
Published online 25 February 2003

MSC (2000) 76D99, 76S05

We consider in this paper the incompressible laminar flow in a porous channel with expanding or contracting walls. While the head-end is closed by a compliant membrane, the downstream end is left unobstructed. For symmetric injection or suction along the uniformly expanding porous walls, the Navier-Stokes equations are reduced to a single, nonlinear, ordinary differential equation. The latter is obtained via similarity transformations in both time and space. The resulting equation is then solved both numerically and asymptotically, using perturbations in the crossflow Reynolds number R. Two separate approaches are presented for each of the injection and suction cases, respectively. For the large injection case, the governing equation is first integrated and the resulting third-order differential equation is solved using the method of variation of parameters. For the large suction case, the governing equation is first simplified near the wall and then solved using successive approximations. Results are then correlated and compared for variations in R and the dimensionless wall expansion rate α. For injection-induced flow, the asymptotic solution becomes more accurate when R/α is increased. Its deviation from the classic sinusoidal profile arising in nonexpanding channels becomes less significant with successive increases in R. For suction-induced flows, faster wall contractions increase the effective Reynolds number $-(\alpha + R)$, thus leading to more precise approximations. For the same absolute value of R, the suction-flow approximation tends to be the most accurate of the two and the least sensitive to variations in α. As $-(\alpha + R)$ is increased, the suction profile approaches the linear form anticipated in nonexpanding channels. By comparison with the injection-induced flow, suction is characterized by improved accuracy, sharper flow turning, and larger shear.

1 Introduction

Studies of porous channel flows have become a recurring topic in fluid mechanics due to the preponderance of related applications. Depending on the application at hand, porous walls have been used in the past to simulate a variety of surface mechanisms. These include natural transpiration, phase sublimation, propellant burning, ablation cooling, and uniformly distributed irrigation. Such mechanisms take place in a number of interesting models of biocirculatory systems, flow filtration, chemical dispensing, rocket propellant combustion, and other membrane separation processes.

Investigations of porous channel flows appear to have been initiated by Berman [1] in his pioneering work that was concerned with the industrial separation of U_{235} from U_{238} by gas diffusion. In fact, by realizing that the normal velocity component must be independent of the streamwise coordinate, Berman was able to reduce the Navier-Stokes equations into a single, nonlinear, fourth-order ODE. His resulting ODE exhibited four boundary conditions and a crossflow Reynolds number R. The latter was based on the normal injection speed $v_{\rm w}$ and the channel half-spacing a. For small R, Berman obtained a regularly perturbed expansion. A number of porous channel-flow studies followed thereafter. These were based on either numerical or theoretical approaches. The latter included the methods of integral analysis, averages, curve-fitting, power-series, matched asymptotic expansions, and multiple scales. The reader may in that regard refer to the works of Taylor [2], Yuan [3], and Terrill [4] (for large injection), Sellars [5] and Terrill [6] (for large suction), Proudman [7] and Shrestha and Terrill [8] (for large and both equal and dissimilar crossflow velocities), Morduchow [9] and White, Barfield, and Goglia [10] (for arbitrary R). Note that Terrill and Shrestha [11] appear to have initiated the study of asymmetric flows caused by different wall permeabilities. Investigations of asymmetric flows and temporal stability issues continue to receive favour in the works of Cox [12], King and Cox [13], Zaturska, Drazin, and Banks [14], Taylor, Banks, Zaturska, and Drazin [15] and Watson, Banks, Zaturska, and Drazin [16, 17]. Recent studies by Cox and King [18], MacGillivray and Lu [19], and Lu [20] are especially useful in unravelling the asymptotic forms of the large suction case.

The spatial stability of steady solutions of the Berman class is another topic that has received much attention in the past. In that respect, one may count Varapaev and Yagodkin [21], Raithby and Knudsen [22], Hocking [23], Sviridenkov and Yagodkin [24], Brady [25], and Durlofsky and Brady [26]. In the same vein, the proof of solution multiplicity over different ranges

* Corresponding author, e-mail: maji@mu.edu

 0044-2267/03/8303-0181 $ 17.50+.50/0

of R has been addressed by Robinson [27], Skalak and Wang [28], Shih [29], Hastings, Lu, and MacGillivray [30], and Lu, MacGillivray, and Hastings [31]. Insofar as injection is concerned, only unique and stable symmetrical solutions were shown to exist for the entire range of the injection Reynolds number. This conclusion was first drawn by Skalak and Wang [28] and was later proved rigorously by Shih [29] and Hastings, Lu, and MacGillivray [30]. For suction flows with $R < -6.0014$, it was shown that at least one of the symmetric solutions could become unstable to two-dimensional asymmetric disturbances and thus bifurcate into a pair of asymmetric solutions. For a thorough investigation of all possible patterns that could accompany suction flows, the reader is referred to Zaturska, Drazin, and Banks [14], and Cox and King [18]. For two and three-dimensional considerations, the reader may also find valuable the articles by Cox [12], King and Cox [13], and Taylor, Banks, Zaturska, and Drazin [15].

In validating the foregoing numerical and theoretical findings, laboratory experiments have also been resorted to. Such investigations simulated, in general, steady channel flows through porous sheets. To name a few, one may cite Taylor [2], Varapaev and Yagodkin [21], Raithby and Knudsen [22], and Sviridenkov and Yagodkin [24]. Overall, these studies have indicated that, in the case of wall injection, asymptotic solutions by Taylor [2], Yuan [3], or Terrill [4] tended to develop rapidly within the channel. For suction, more than one solution could be observed, with one corresponding to the simple approximation given by Sellars [5] and Terrill [6].

The purpose of this paper is to extend previous investigations by presenting theoretical solutions for both large injection and suction in a porous channel with expanding or contracting walls. To make headway, we shall limit our scope to symmetric solutions only. In the suction case, the reader is cautioned that our model does not consider asymmetric solutions that may physically exist. As reported by Cox and King [18] (p. 712), all solutions with symmetric boundary conditions were, in the past, assumed to possess symmetry about the midsection plane of the channel. However, this perception was changed when Zaturska, Drazin, and Banks [14] showed that asymmetric solutions could emerge from a pitchfork bifurcation of a large suction solution. The asymmetric forms were later confirmed and completed by Cox and King [18]. In these studies, two symmetric solutions for large suction were shown to possess a common leading order term ([14], p. 165). In the current work, the same inviscid term will be reproducible from the forthcoming generalization when the porous walls are made motionless. In later work, we hope to address the other possible solutions for large suction.

A principal objective of the current study is to overcome deficiencies in practical models that do not account for wall motion, viscous diffusion, or both. For example, in modelling the gas dynamics produced by solid propellant combustion, previous studies have ignored both viscosity and propellant regression by relying on Taylor's inviscid profile. Recent studies by Apte and Yang [32], Lee and Beddini [33, 34], Flandro and Majdalani [35], and others have indicated the importance of retaining viscous corrections due to their appreciable contribution to the damping of vorticity waves. Thus, not only does viscosity alter the mean flow character, but it also affects the assessment of motor stability that is strongly influenced by vortical energy. Besides its impact on aeroacoustic instability, retention of the viscous Reynolds number in the mean flow description makes it possible to formulate a consistently viscous and rotational solution in both mean and unsteady parts. This enables us to refine, along those lines, the aeroacoustic solution presented recently by Majdalani and Roh [36]; therein viscous effects were included in the vortico-acoustic equations but ignored in Taylor's mean flow expression. While viscous corrections are clearly beneficial, retention of wall regression improves our capability to model fast burning propellants developed for high-acceleration vehicles [37, 38]. It also improves our ability to capture the ablating surface during transpiration cooling of re-entry vehicles and solid rocket boosters [39]. It is equally useful in simulating the sublimation process of a solidified gas that is often used to mimic the regression of a solid propellant [40–42]. Although idealized rocket motors possess circular cross-sections, the channel flow geometry associated with a slab rocket motor has become no less popular in recent years. In fact, one may cite numerous experimental [40–47] and theoretical investigations [45–50] concerned with such geometry. This may be partly attributed to the fact that planar configurations are advantageous in facilitating flow visualization in a windowed environment.

From a different perspective, the sequence of expansions and contractions completed by channel walls can enable a researcher to mimic more realistically peristaltic motion caused by pulsating walls and involving fluid absorption [51, 52]. It thus provides procedural tools that can help physiologists interested in modelling seepage and filtration processes [53–55]. This is due to the role played by filtration in many parts of the body besides its considerable use in extracorporeal processing of fluids and mixtures [1]. While filtration in biological organisms is often studied in long circular 'tubules,' extracorporeal duct flows take place more commonly between parallel flat membranes. The corresponding 'slit flow' in a narrow channel with compliant membranes is, of course, a subset of the forthcoming generalization.

To reduce the Navier-Stokes equations, we shall first combine the procedural tools found in Berman [1], Yuan [3], Sellars [5], Terrill [6], and Goto and Uchida [52]. Using similarity transformations in both space and time we shall employ a linearly varying axial velocity and a uniform expansion (or contraction) ratio. This will reduce the Navier-Stokes equations into a single nonlinear equation that can be solved both numerically and asymptotically. Depending on whether injection or suction is present, two separate asymptotic procedures will be implemented to arrive at closed-form approximations. By making the walls motionless, our solutions will be shown to embrace previous formulations as one may restore, from ours, either Yuan's [3] or Sellars' [5] for the large injection and suction cases, respectively. From the asymptotic solutions, closed-form expressions will be obtained for the velocity, pressure, and shear stresses. These will be collectively used to characterize the flow. Furthermore, comparisons with numerical solutions will be called upon to verify the accuracy of the asymptotic formulations over a wide range of moderate-to-high Reynolds numbers.

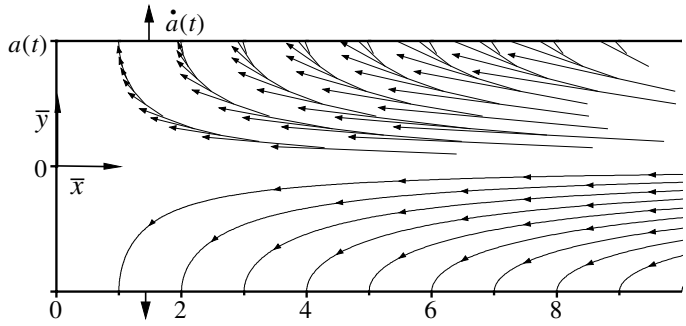

Fig. 1 Two-dimensional channel with expanding (or contracting) porous walls. Vector and streamline plots are depicted in the opposing halves of the solution domain.

2 Mathematical model

A porous plenum or chamber can be modelled as a channel with a rectangular cross section. In this study, one side of the cross section, representing the distance $2a$ between the porous walls is taken to be smaller than the other two. This enables us to treat the problem as a case of two-dimensional flow. Both sidewalls are assumed to have equal permeability and to expand or contract uniformly at a time-dependent rate $\dot{a}$. Insofar as the body length L is unrestricted, one may assume a semi-infinite length [51]. In order to accommodate expanding boundaries, the head end is closed by a compliant membrane that is allowed to stretch with channel expansion. At the downstream end, the channel is fully open.

As shown in Fig. 1, a coordinate system may be chosen with the origin at the centre of the channel. Using the over-bar in some cases to denote dimensional variables, we let $\overline{x}$ and $\overline{y}$ be the axial and normal coordinates. The corresponding axial and normal velocity components are defined as $\overline{u}$ and $\overline{v}$. For uniform wall injection and no flow across the midsection plane, symmetry may be used to limit the investigation over half of the channel ($0 \le \bar{y} \le a$).

For two-dimensional laminar and incompressible flow with no body forces, the differential expressions for mass and momentum conservation can be written as

$$\frac{\partial \overline{u}}{\partial \overline{x}} + \frac{\partial \overline{v}}{\partial \overline{y}} = 0, \tag{1}$$

$$\frac{\partial \overline{u}}{\partial t} + \overline{u}\frac{\partial \overline{u}}{\partial \overline{x}} + \overline{v}\frac{\partial \overline{u}}{\partial \overline{y}} = -\frac{1}{\rho}\frac{\partial \overline{p}}{\partial \overline{x}} + \nu\left(\frac{\partial^2 \overline{u}}{\partial \overline{x}^2} + \frac{\partial^2 \overline{u}}{\partial \overline{y}^2}\right), \tag{2}$$

$$\frac{\partial \overline{v}}{\partial t} + \overline{u}\frac{\partial \overline{v}}{\partial \overline{x}} + \overline{v}\frac{\partial \overline{v}}{\partial \overline{y}} = -\frac{1}{\rho}\frac{\partial \overline{p}}{\partial \overline{y}} + \nu\left(\frac{\partial^2 \overline{v}}{\partial \overline{x}^2} + \frac{\partial^2 \overline{v}}{\partial \overline{y}^2}\right), \tag{3}$$

where ρ, ν, $\overline{p}$, and t are the dimensional density, kinematic viscosity, pressure, and time. The boundary conditions are

$$\overline{u}(\bar{x}, a) = 0, \quad \overline{v}(a) = -v_{\mathrm{w}} = -A\dot{a}, \tag{4}$$

$$\frac{\partial \overline{u}}{\partial \overline{y}}(\bar{x}, 0) = 0, \quad \overline{v}(0) = 0, \quad \overline{u}(0, \bar{y}) = 0. \tag{5}$$

At the wall, it is assumed that the fluid inflow velocity v_{w} is independent of position. Additionally, the injection coefficient ($A \equiv v_{\mathrm{w}}/\dot{a}$) that appears in eq. (4) is a measure of wall permeability.

At this point, the Stokes stream function may be introduced. This is accomplished via

$$\bar{u} = \frac{\partial \bar{\psi}}{\partial \bar{y}}, \quad \bar{v} = -\frac{\partial \bar{\psi}}{\partial \bar{x}}. \tag{6}$$

Pressure can also be eliminated from the momentum equation by transforming it into the vorticity transport equation given by

$$\frac{\partial \bar{\zeta}}{\partial t} + \bar{u}\frac{\partial \bar{\zeta}}{\partial \bar{x}} + \bar{v}\frac{\partial \bar{\zeta}}{\partial \bar{y}} = \nu\left(\frac{\partial^2 \bar{\zeta}}{\partial \bar{x}^2} + \frac{\partial^2 \bar{\zeta}}{\partial \bar{y}^2}\right), \tag{7}$$

where

$$\bar{\zeta} = \frac{\partial \bar{v}}{\partial \bar{x}} - \frac{\partial \bar{u}}{\partial \bar{y}}. \tag{8}$$

3 Reduction of the flow equations

3.1 Similar solution in space

In view of the boundary conditions given by eqs. (4) and (5), a similar solution can be developed from the mean flow stream function. Defining the dimensionless normal coordinate to be $y \equiv \bar{y}/a$, the stream function can be written as

$$\bar{\psi} = \nu h(a)\bar{x}\bar{F}(y,t), \tag{9}$$

where $\bar{F}(y,t)$ is independent of the axial coordinate, and $h(a)$ is some subsidiary function. Inserting eq. (9) into eq. (6), the axial and normal velocities can be expressed as

$$\bar{u} = \frac{\nu\bar{x}}{a}h(a)\bar{F}_y, \quad \bar{v} = -\nu h(a)\bar{F}(y,t), \tag{10}$$

where $\bar{F}_y = \partial\bar{F}/\partial y$. Due to the linear spatial dependence, we have $\bar{u}_{\bar{x}\bar{x}} = \bar{v}_{\bar{x}} = 0$. As $\bar{v}$ is independent of $\bar{x}$, the vorticity equation reduces to

$$\bar{\zeta} = -\frac{\partial\bar{u}}{\partial\bar{y}}, \tag{11}$$

whereby eq. (3) collapses into $\bar{p}_{\bar{y}\bar{x}} = 0$. Upon substitution into eq. (7), one obtains

$$\bar{u}_{\bar{y}t} + \bar{u}\bar{u}_{\bar{y}\bar{x}} + \bar{v}\bar{u}_{\bar{y}\bar{y}} = \nu\bar{u}_{\bar{y}\bar{y}\bar{y}}. \tag{12}$$

Inserting eq. (10) into eq. (12) gives

$$\left[\frac{\nu\bar{x}}{a^2}h(a)\bar{F}_{yy}\right]_t + \frac{\nu^2\bar{x}}{a^3}h^2(a)\bar{F}_y\bar{F}_{yy} - \frac{\nu^2\bar{x}}{a^3}h^2(a)\bar{F}\bar{F}_{yyy} = \frac{\nu^2\bar{x}}{a^4}h(a)\bar{F}_{yyyy}. \tag{13}$$

This equation will be dimensionally homogeneous if, and only if

$$\frac{\nu^2\bar{x}}{a^3}h^2(a) \sim \frac{\nu^2\bar{x}}{a^4}h(a) \quad \text{or} \quad h(a) = a^{-1}. \tag{14}$$

The axial and normal velocities become

$$\bar{u} = \frac{\nu\bar{x}}{a^2}\bar{F}_y, \quad \text{and} \quad \bar{v} = -\frac{\nu}{a}\bar{F}(y,t). \tag{15}$$

3.2 Governing equation

In order to solve eq. (12), one must start by evaluating its partial derivatives. Using $y = \bar{y}/a$ and applying the chain rule to eq. (15), one obtains

$$\bar{u}_{\bar{y}} = \left(\frac{\nu\bar{x}}{a^2}\bar{F}_y\right)_y\frac{\partial y}{\partial\bar{y}} = \frac{\nu\bar{x}}{a^3}\bar{F}_{yy}. \tag{16}$$

In turn, partial derivatives change into

$$\bar{u}_{\bar{y}\bar{x}} = \frac{\nu}{a^3}\bar{F}_{yy}, \quad \bar{u}_{\bar{y}\bar{y}} = \frac{\nu\bar{x}}{a^4}\bar{F}_{yyy}, \quad \bar{u}_{\bar{y}\bar{y}\bar{y}} = \frac{\nu\bar{x}}{a^5}\bar{F}_{yyyy}. \tag{17}$$

Recalling that y and a are time-dependent, one may evaluate $\bar{u}_{\bar{y}t}$ from

$$\bar{u}_{\bar{y}t} = \left(\frac{\nu\bar{x}}{a^3}\bar{F}_{yy}\right)_t = \frac{\nu\bar{x}}{a^3}\bar{F}_{yyt} + \frac{\nu\bar{x}}{a^3}\bar{F}_{yyy}\frac{\partial y}{\partial t} - \frac{3\nu\bar{x}\dot{a}}{a^4}\bar{F}_{yy}; \quad \frac{\partial y}{\partial t} = -\frac{\dot{a}y}{a}. \tag{18}$$

Therefore,

$$\bar{u}_{\bar{y}t} = \frac{\nu\bar{x}}{a^3}\bar{F}_{yyt} - \frac{\nu\bar{x}\dot{a}}{a^4}y\bar{F}_{yyy} - \frac{3\nu\bar{x}\dot{a}}{a^4}\bar{F}_{yy}. \tag{19}$$

When substituting eq. (17) and eq. (19) into eq. (12), a differential equation is developed for $\bar{F}$. This is

$$\bar{F}_{yyyy} + \alpha\left(y\bar{F}_{yyy} + 3\bar{F}_{yy}\right) + \bar{F}\bar{F}_{yyy} - \bar{F}_y\bar{F}_{yy} - a^2\nu^{-1}\bar{F}_{yyt} = 0, \tag{20}$$

where α is the wall expansion ratio defined by

$$\alpha \equiv \frac{\dot{a}a}{\nu}. \tag{21}$$

Note that the expansion ratio will be positive for expansion and negative for contraction. A careful integration of eq. (20) produces

$$\bar{F}_{yyy} + \alpha\left(y\bar{F}_{yy} + 2\bar{F}_y\right) + \bar{F}\bar{F}_{yy} - \left(\bar{F}_y\right)^2 - a^2\nu^{-1}\bar{F}_{yt} = \lambda, \tag{22}$$

where λ is a space-invariant parameter. The boundary conditions given by eqs. (4)–(5) translate into

$$\bar{F}_{yy}(0) = 0,\ \bar{F}(0) = 0,\ \bar{F}_y(1) = 0,\ \bar{F}(1) = R, \tag{23}$$

where R is the crossflow Reynolds number defined by $R \equiv av_{\mathrm{w}}/\nu$. Note that R is positive for injection and negative for suction. Quantities expressed by eqs. (9), (15), (20), and (23) can be normalized via

$$\psi = \frac{\bar{\psi}}{av_{\mathrm{w}}}, \quad u = \frac{\overline{u}}{v_{\mathrm{w}}}, \quad v = \frac{\overline{v}}{v_{\mathrm{w}}}, \quad x = \frac{\overline{x}}{a}, \quad F = \frac{\overline{F}}{R}, \tag{24}$$

where F is the characteristic mean flow function. When this dimensionless set is used, the normalized equations become

$$\psi = xF, \tag{25}$$

$$u = xF_y, \quad v = -F, \tag{26}$$

$$R^{-1}F_{yyy} + \alpha R^{-1}\left(yF_{yy} + 2F_y\right) + FF_{yy} - \left(F_y\right)^2 - \left(a/v_{\mathrm{w}}\right)F_{yt} = \lambda \tag{27}$$

with

$$F_{yy}(0) = 0, \quad F(0) = 0, \quad F_y(1) = 0, \quad F(1) = 1. \tag{28}$$

3.3 Similar solution in space and time

A similar solution with respect to both space and time can now be developed by precisely following the transformation described by Uchida and Aoki [51]. For constant α and $F = F(y)$, it follows that $F_{yyt} = 0$. To realize this condition, the value of the expansion ratio α must be specified by its initial value

$$\alpha = \frac{\dot{a}a}{\nu} = \frac{\dot{a}_0 a_0}{\nu} = \text{constant}, \text{ or } \frac{\dot{a}_0}{\dot{a}} = \frac{a}{a_0}, \tag{29}$$

where a_0 and $\dot{a}_0$ denote the initial channel height and expansion rate. Forthwith, the temporal similarity transformation can be achieved by integrating eq. (29) with respect to time. The result is

$$a/a_0 = \sqrt{1 + 2\nu\alpha t a_0^{-2}}. \tag{30}$$

Since $v_{\mathrm{w}} = A\dot{a}$, an expression for the injection velocity variation can be determined, provided that the injection coefficient A is constant. From eqs. (29) and (30), it is clear that

$$\frac{\dot{a}_0}{\dot{a}} = \frac{v_{\mathrm{w}}(0)}{v_{\mathrm{w}}(t)} = \sqrt{1 + 2\nu\alpha t a_0^{-2}}. \tag{31}$$

Under these provisions, eq. (27) becomes

$$R^{-1}F''' + \alpha R^{-1}\left(yF'' + 2F'\right) + FF'' - \left(F'\right)^2 = \lambda, \tag{32}$$

where a prime denotes differentiation with respect to y. The exact solution becomes contingent upon finding an F that satisfies

$$F''(0) = 0, \quad F(0) = 0, \quad F'(1) = 0, \quad F(1) = 1. \tag{33}$$

Note that Berman's classic equation [1] is a special case of eq. (32) that can be obtained by suppressing α.

4 Solution for the large injection case

For moderate-to-large values of the positive Reynolds number, eq. (32) can be solved asymptotically. For that purpose, we define $\varepsilon \equiv R^{-1}$ to be our perturbation parameter. The problem becomes that of solving

$$\varepsilon F''' + \alpha\varepsilon\left(yF'' + 2F'\right) + FF'' - \left(F'\right)^2 = \lambda, \tag{34}$$

where a small parameter multiplies the highest derivative. Evidently, a regular perturbation expansion of the form $F = F_0 + \varepsilon F_1 + O(\varepsilon^2)$, $\lambda = \lambda_0 + \varepsilon\lambda_1$ can be attempted. When substituted into eq. (34), this expansion yields, at $O(1)$,

$$F_0F_0'' - \left(F_0'\right)^2 = \lambda_0, \tag{35}$$

with $F_0'(1) = 0,\ F_0(1) = 1,\ F_0(0) = 0$. It can be easily verified that the leading order solution is $F_0 = \sin\theta$, where $\theta = \frac{1}{2}\pi y$ and $\lambda_0 = -\frac{1}{4}\pi^2$.

4.1 First-order solution in θ

Terms of $O(\varepsilon)$ can be gathered and separated. The emerging first-order equation becomes

$$F_0F_1'' - 2F_0'F_1' + F_0''F_1 = -F_0'''' - 2\alpha F_0' - \alpha yF_0'' + \lambda_1. \tag{36}$$

This needs to be solved while satisfying

$$F_1'(1) = 0,\ F_1(1) = 0,\ F_1(0) = 0. \tag{37}$$

Switching to θ as the independent variable, and using $F_0 = \sin\theta$, eq. (36) can be written as

$$\sin\theta F_1'' - 2\cos\theta F_1' - \sin\theta F_1 = (\tfrac{1}{2}\pi - 4\alpha/\pi)\cos\theta + (2\alpha/\pi)\theta\sin\theta + \lambda_2, \quad \lambda_2 = -4\pi^{-2}\lambda_1 \tag{38}$$

with

$$F_1'\left(\tfrac{1}{2}\pi\right) = 0,\ F_1\left(\tfrac{1}{2}\pi\right) = 0,\ F_1(0) = 0. \tag{39}$$

4.2 Solving by variation of parameters

The solution of eq. (38) must be carefully constructed. First, one can attempt to solve the homogeneous equation

$$\sin\theta F_1'' - 2\cos\theta F_1' - \sin\theta F_1 = 0. \tag{40}$$

To that end, one independent solution exhibited by eq. (40) can be guessed to be

$$F_{1H} = \cos\theta. \tag{41}$$

Having determined one independent solution, the method of variation of parameters may be employed. This requires setting

$$F_{1H} = K(\theta)\cos\theta, \tag{42}$$

where $K(\theta)$ is unknown. Differentiation gives

$$F_{1H}' = K'\cos\theta - K\sin\theta, \tag{43}$$

$$F_{1H}'' = K''\cos\theta - 2K'\sin\theta - K\cos\theta. \tag{44}$$

Substitution into eq. (40) yields

$$K''\sin 2\theta - 4K' = 0 \tag{45}$$

or

$$K(\theta) = K_0\left(\tan\theta - \theta\right) + K_1, \tag{46}$$

where K_0 and K_1 are integration parameters. This completes the expression for the general homogeneous solution

$$F_{1H} = K_0\left(\sin\theta - \theta\cos\theta\right) + K_1\cos\theta. \tag{47}$$

According to the method of variation of parameters, the two constants K_0 and K_1 must be allowed to vary with θ once more. At the outset, eq. (47) becomes

$$F_1(\theta) = K_0(\theta)\left(\sin\theta - \theta\cos\theta\right) + K_1(\theta)\cos\theta. \tag{48}$$

The last term needs to be differentiated twice before being substituted into eq. (38). The first differentiation yields

$$F_1' = K_0'\left(\sin\theta - \theta\cos\theta\right) + K_0\theta\sin\theta + K_1'\cos\theta - K_1\sin\theta. \tag{49}$$

4.3 Parametric constraint

At this point, a procedural constraint that binds the derivatives of the variable parameters must be imposed. Our choice is guided by conventional theory that suggests setting

$$K_0' \left(\sin\theta - \theta\cos\theta\right) + K_1' \cos\theta = 0. \tag{50}$$

Eq. (49) becomes

$$F_1' = K_0 \theta \sin\theta - K_1 \sin\theta, \tag{51}$$

whose derivative gives

$$F_1'' = K_0'\theta\sin\theta + K_0\left(\sin\theta + \theta\cos\theta\right) - K_1'\sin\theta - K_1\cos\theta. \tag{52}$$

We now put F_1 and its derivatives, given by eqs. (48), (51), and (52), back into the complete first-order equation, given by eq. (38). The result is

$$K_0'\theta\sin^2\theta - K_1'\sin^2\theta = \left(\tfrac{1}{2}\pi - 4\alpha/\pi\right)\cos\theta + (2\alpha/\pi)\theta\sin\theta + \lambda_2. \tag{53}$$

Eq. (53) contains two unspecified functions, K_0' and K_1'. In order to obtain closure, the constraint introduced in eq. (50) must be employed alongside eq. (53). At length, we find that

$$K_0'(\theta) = \left[\left(\tfrac{1}{2}\pi - 4\alpha/\pi\right)\cot\theta + (2\alpha/\pi)\theta + \lambda_2\csc\theta\right]\cot\theta\csc\theta, \tag{54}$$

$$K_1'(\theta) = \left[(2\alpha/\pi)\theta + \left(\tfrac{1}{2}\pi - 4\alpha/\pi\right)\cot\theta + \lambda_2\csc\theta\right](\theta\cot\theta - 1)\csc\theta. \tag{55}$$

By integrating for the variable parameters, one obtains

$$K_0(\theta) = \left(2\alpha/\pi - \tfrac{1}{4}\pi\right)\cos\theta\csc^2\theta + \left(4\alpha/\pi - \tfrac{1}{4}\pi\right)\ln\tan(\tfrac{1}{2}\theta) - (2\alpha/\pi)\theta\csc\theta - (\lambda_2/\pi)\csc^2\theta + c_0, \tag{56}$$

$$K_1(\theta) = \left(2\alpha/\pi - \tfrac{1}{4}\pi\right)(\theta\cot\theta - 1)\csc\theta + \left(4\alpha/\pi - \tfrac{1}{4}\pi\right)S(\theta) - (2\alpha/\pi)\theta^2\csc\theta + \tfrac{1}{2}\lambda_2\left(\cot\theta - \theta\csc^2\theta\right) + c_1, \tag{57}$$

where c_0 and c_1 are constants and

$$S(\theta) \equiv \int_0^\theta \phi\csc\phi\,\mathrm{d}\phi. \tag{58}$$

Inserting eqs. (56)–(57) into eq. (48) yields

$$F_1 = -2\alpha\theta/\pi + \left(4\alpha/\pi - \tfrac{1}{4}\pi\right)\left[(\sin\theta - \theta\cos\theta)\ln\tan\tfrac{1}{2}\theta + \cos\theta S(\theta)\right] + \left(c_0 - \tfrac{1}{2}\lambda_2\right)\sin\theta - c_0\theta\cos\theta + c_1\cos\theta. \tag{59}$$

Applying the three boundary conditions given by eq. (39) and making use of $S(0) = 0$, the two constants c_0 and c_1 can be determined in addition to the parameter λ_2. One finds

$$\begin{aligned} c_0 &= \tfrac{1}{2} - 4\alpha\pi^{-2} + \left(8\alpha\pi^{-2} - \tfrac{1}{2}\right)S\left(\tfrac{1}{2}\pi\right), \quad c_1 = 0, \\ \lambda_2 &= 2\left(c_0 + \alpha\right) = 2\alpha + 1 - 8\alpha\pi^{-2} + \left(16\alpha\pi^{-2} - 1\right)S\left(\tfrac{1}{2}\pi\right). \end{aligned} \tag{60}$$

The first-order solution is, finally,

$$\begin{aligned} F_1 \;=\; & -2\alpha\theta/\pi + (\tfrac{1}{4}\pi - 4\alpha/\pi)\left[(\theta\cos\theta - \sin\theta)\ln\tan\tfrac{1}{2}\theta - \cos\theta S(\theta)\right] + \alpha\sin\theta \\ & + \left[\left(\tfrac{1}{2} - 8\alpha\pi^{-2}\right)S\left(\tfrac{1}{2}\pi\right) + 4\alpha\pi^{-2} - \tfrac{1}{2}\right]\theta\cos\theta. \end{aligned} \tag{61}$$

4.4 Complete solution

The first-order corrections appearing in eq. (61) can be combined with the leading order solution. For added clarity, the resulting function and its derivatives are reproduced below at $O(\varepsilon^2)$

$$\begin{aligned} F(\theta) \;=\; & \sin\theta + \varepsilon\left\{-2\alpha\theta/\pi + (\tfrac{1}{4}\pi - 4\alpha/\pi)\left[(\theta\cos\theta - \sin\theta)\ln\tan\tfrac{1}{2}\theta + \cos\theta S(\theta)\right] + \alpha\sin\theta \right. \\ & \left. + \left[\left(\tfrac{1}{2} - 8\alpha\pi^{-2}\right)S\left(\tfrac{1}{2}\pi\right) + 4\alpha\pi^{-2} - \tfrac{1}{2}\right]\theta\cos\theta\right\}, \end{aligned} \tag{62}$$

$$\begin{aligned} F'(\theta) \;=\; & \cos\theta + \varepsilon\left\{2\alpha/\pi - \tfrac{1}{4}\pi + (\tfrac{1}{4}\pi - 4\alpha/\pi)\left[\sin\theta S(\theta) - \theta\sin\theta\ln\tan\tfrac{1}{2}\theta\right] + \alpha\cos\theta \right. \\ & \left. + \left[\left(\tfrac{1}{2} - 8\alpha\pi^{-2}\right)S\left(\tfrac{1}{2}\pi\right) + 4\alpha\pi^{-2} - \tfrac{1}{2}\right](\cos\theta - \theta\sin\theta)\right\}, \end{aligned} \tag{63}$$

$$F''(\theta) = -\sin\theta + \varepsilon\left\{\left(\tfrac{1}{4}\pi - 4\alpha/\pi\right)\left[\cos\theta S(\theta) - (\sin\theta + \theta\cos\theta)\ln\tan\tfrac{1}{2}\theta\right] - \alpha\sin\theta - \left[\left(\tfrac{1}{2} - 8\alpha\pi^{-2}\right)S\left(\tfrac{1}{2}\pi\right) + 4\alpha\pi^{-2} - \tfrac{1}{2}\right](2\sin\theta + \theta\cos\theta)\right\}, \quad (64)$$

$$F'''(\theta) = -\cos\theta + \varepsilon\left\{\left(\tfrac{1}{4}\pi - 4\alpha/\pi\right)\left[-\sin\theta S(\theta) - (2\cos\theta - \theta\sin\theta)\ln\tan\tfrac{1}{2}\theta - 1\right] - \alpha\cos\theta - \left[\left(\tfrac{1}{2} - 8\alpha\pi^{-2}\right)S\left(\tfrac{1}{2}\pi\right) + 4\alpha\pi^{-2} - \tfrac{1}{2}\right](3\cos\theta - \theta\sin\theta)\right\}. \quad (65)$$

Note that, following eq. (38), primes have been used to denote differentiation with respect to θ. When reverting back to y, one must use $F = F(\frac{1}{2}\pi y)$, $F_y = \frac{1}{2}\pi F'(\theta)$, $F_{yy} = \frac{1}{4}\pi^2 F''(\theta)$, $F_{yyy} = \frac{1}{8}\pi^3 F'''(\theta)$. At present, it is reassuring to recognize that eq. (62) reduces to Yuan's formulation [3] by setting $\alpha = 0$, and to Taylor's [2] by setting $\varepsilon = 0$.

5 Solution for the large suction case

For the large suction case, R is a large negative number and the location of the boundary layer is shifted across the domain. It is therefore necessary to rewrite the governing equation and its boundary conditions. Using primes to denote differentiation with respect to y, one may begin with

$$R^{-1}F''' + \alpha R^{-1}(yF'' + 2F') + FF'' - (F')^2 = \lambda. \quad (66)$$

By letting $z = 1 - y$, eqs. (66) and (33) can be rewritten as

$$-F''' + \alpha(F'' - zF'' - 2F') + R\left[FF'' - (F')^2\right] = k, \quad (67)$$

$$F''(1) = 0,\ F(1) = 0,\ F'(0) = 0,\ F(0) = 1, \quad (68)$$

where k is a constant and the prime has been reassigned to z. Since the suction flow is dominated by events that take place near the wall, a first approximation to eq. (67) can be obtained near $z = 0$ by utilizing the corresponding boundary conditions in eq. (68). Thus we find

$$F''' + MF'' = -k, \quad (69)$$

where $M \equiv -(\alpha + R)$ is a large positive number. In a standard boundary-layer treatment, (69) would be written in the form $\sum F_j \exp(-Mz)$ and then solved from boundary conditions at the wall and at infinity. An 'outer' solution is then carefully determined and superimposed to obtain a uniformly valid expansion. In the current problem, we find the outer solution to be 'one'. Instead, a series solution is obtained in a manner to satisfy all four conditions in (68). To see this, it is helpful to examine the leading order solution to eqs. (68)–(69):

$$F(z) = 1 + C\left[\tfrac{1}{2}M^2z^2\mathrm{e}^{-M} + 1 - \mathrm{e}^{-Mz} - Mz\right], \quad (70)$$

where

$$C = \frac{1}{(M-1) + \mathrm{e}^{-M}(1 - \frac{1}{2}M^2)}. \quad (71)$$

Surely, the presence of Mz and $M^2z^2\mathrm{e}^{-M}$ can lead to a divergent solution at sufficiently large z. For large M, however, $M^j\mathrm{e}^{-M}$ is close to zero, $\forall j$; this suggests an expansion of the form

$$F(z) = 1 + \sum_{j=1}^{\infty}(M-1)^{-j}F_j(z). \quad (72)$$

We find that, by keeping the first three terms only, a simple and accurate solution is obtained. The corresponding perturbation expansion can be constructed from

$$F(z) = 1 + (M-1)^{-1}\left(1 - \mathrm{e}^{-Mz} - Mz\right) + (M-1)^{-2}F_2(z). \quad (73)$$

where $F_2(z)$ must be determined. Forthwith, one can insert eq. (73) into eq. (67) and collect terms of order $(M-1)^{-2}$. One finds

$$F_2''' + MF_2'' = M^3\left(-Mz\mathrm{e}^{-Mz} - \mathrm{e}^{-Mz}\right) + k_2, \quad (74)$$

where k_2 is a constant. At this order, the boundary conditions become

$$F_2''(1) = 0,\ F_2(1) = 0,\ F_2'(0) = 0,\ F_2(0) = 0. \tag{75}$$

Direct integration yields

$$F_2 = \left(-\tfrac{1}{2}M^2z^2 - 3Mz\right)\mathrm{e}^{-Mz} + \frac{3M}{M-1}\left(1 - z - \mathrm{e}^{-Mz}\right), \tag{76}$$

wherefrom

$$F(z) = 1 + (M-1)^{-1}\left(1 - \mathrm{e}^{-Mz} - Mz\right) - (M-1)^{-2}\mathrm{e}^{-Mz}\left(\tfrac{1}{2}M^2z^2 + 3Mz\right) + 3(M-1)^{-3}M\left(1 - z - \mathrm{e}^{-Mz}\right). \tag{77}$$

Principal derivatives include

$$F'(z) = M(M-1)^{-1}\left(\mathrm{e}^{-Mz} - 1\right) + (M-1)^{-2}\mathrm{e}^{-Mz}\left(\tfrac{1}{2}M^3z^2 + 2M^2z - 3M\right) + 3M(M-1)^{-3}\left(M\mathrm{e}^{-Mz} - 1\right), \tag{78}$$

$$F''(z) = -M^2(M-1)^{-1}\mathrm{e}^{-Mz} + (M-1)^{-2}\mathrm{e}^{-Mz}\left(3M^3z + 2M^2z + 5M^2 - \tfrac{1}{2}M^4z^2\right) - 3M^3(M-1)^{-3}\mathrm{e}^{-Mz}, \tag{79}$$

$$F'''(z) = M^3(M-1)^{-1}\mathrm{e}^{-Mz} + M^2(M-1)^{-2}\mathrm{e}^{-Mz}\left(2 - 2M - 4M^2z + 2Mz - \tfrac{1}{2}M^3z^2\right) + 3M^4(M-1)^{-3}\mathrm{e}^{-Mz}. \tag{80}$$

Recalling that $F'(y) = -F'(z)$, $F''(y) = F''(z)$, and $F'''(y) = -F'''(z)$, the derivatives in terms of y are at hand. It is interesting to note that the solution given originally by Sellars [5] and later improved by Terrill [6] can be reproduced from eq. (77) by setting $\alpha = 0$.

6 The velocity field

A numerical solution for eqs. (32)–(33) can be readily obtained using a shooting method in conjunction with a seventh-order Runge-Kutta solver. The step size can be chosen to be sufficiently small to produce true values in at least 8 significant digits. With such negligible error, the numerical solution can be used as a benchmark for comparisons with the moderate-to-large suction and injection approximations. This can be performed over a range of crossflow Reynolds numbers and wall expansion rates.

6.1 Normal velocity for constant expansion and contraction rates

Both numeric and asymptotic plots of the normal velocity v (or $-F$) are now shown in Fig. 2 for constant wall expansion ($\alpha = 10$, Fig. 2a) and contraction ($\alpha = -10$, Fig. 2b). In both figures, the solution appears to be sinusoidal for injection and linear for suction. Such behaviour is consistent with Yuan's [3] and Sellars' [5] solutions in the absence of wall motion. Wall motion seems to produce a small additional deviation or shifting from the stationary wall solution. While wall expansion appears to enhance the effect of suction, wall contraction is seen to increase the effective injection Reynolds number. This can be illustrated by comparing the suction plots in Figs. 2a and 2b. Since $\alpha = 10$ in Fig. 2a, the Reynolds numbers of -50 and -100 lead to effective suction Reynolds numbers (i.e., $M = -(R + \alpha)$ in eq. (69)) of 40 and 90. In Fig. 2b, the effective Reynolds numbers become 60 and 110. Insofar as the solution sensitivity to α diminishes at higher suction levels, the spacing between suction curves is reduced in Fig. 2b. Overall, wall contraction is found to accelerate asymptotic convergence in the suction case, whereas expansion seems to accelerate convergence in the wall injection formulation. The magnified portions of the graph indicate that asymptotics and numerics coincide for $R \leq -50$ and $R \geqslant 500$. For this reason, theoretical and numerical solutions become indistinguishable outside the range $-50 \leq R \leq 500$. Since the accuracy associated with the asymptotic expressions improves at higher effective Reynolds numbers, our models may be quite appropriate in the modelling of both hard-blowing and hard-suction surface phenomena.

6.2 Axial velocity for constant expansion and contraction rates

For the same range of R and α, the self-similar axial velocity u/x is now plotted in Fig. 3. By comparison to Fig. 2, similar conclusions can be drawn. For instance, it can be seen that the injection velocity approaches the cosine profile predicted by Yuan [3] while the suction profile becomes progressively flatter as it approaches the plug pattern predicted by Sellars [5] in the absence of wall motion. Here too, the agreement between asymptotics and numerics improves at higher effective Reynolds numbers. In general, this agreement is less apparent near the core where a viscous boundary layer involving exponentially small terms is believed to exist (cf. Terrill [56]). While contraction in Fig. 3b increases the net suction level (and therefore convergence), it leads to a more noticeable discrepancy between asymptotics and numerics in the injection case (e.g., $R = 50$).

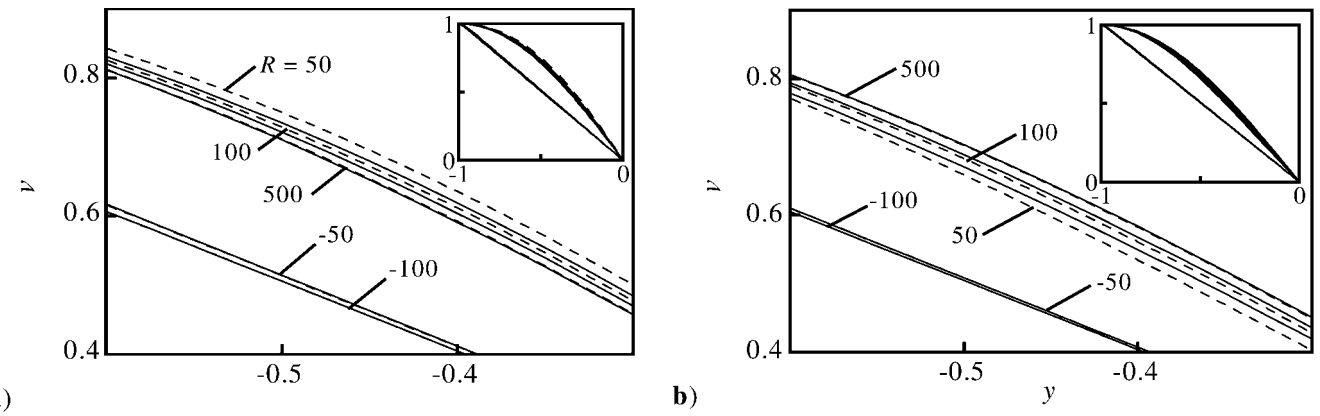

Fig. 2 Comparison between numeric (—) and asymptotic (- - -) solutions for v at a) $\alpha = 10$, and b) $\alpha = -10$; $-100 \leq R \leq 500$.

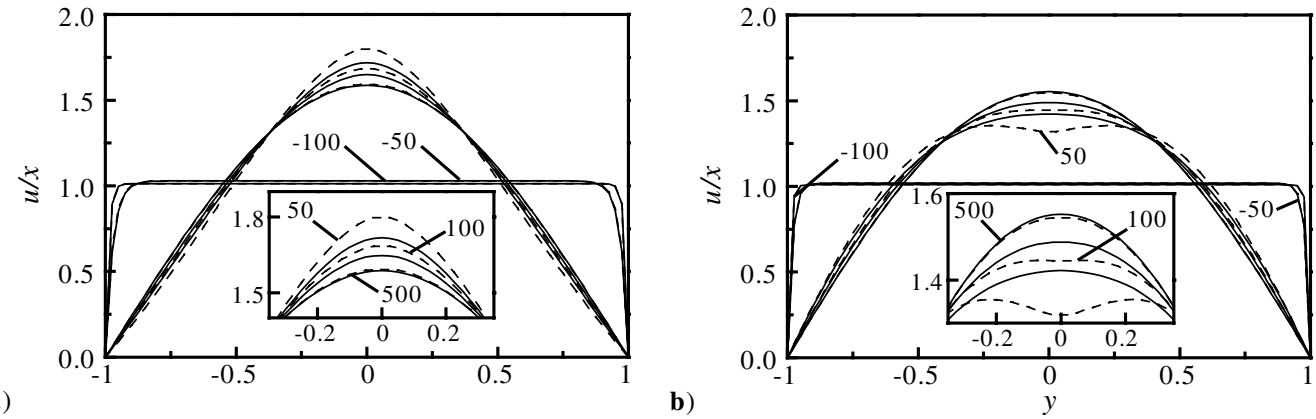

Fig. 3 Comparison between numeric (—) and asymptotic (- - -) solutions for u/x at a) $\alpha = 10$, and b) $\alpha = -10$; $-100 \leq R \leq 500$.

As far as minimizing the asymptotic error is concerned, contraction appears to be favourable for suction (since it increases M) and adverse for injection.

The small boundary layer at the core is clearly induced by wall injection. As one would expect, it is 'blown off' the porous wall by the convective action of the incoming stream (Cole and Aroesty [57]). Surely it becomes smaller with successive increases in R. This explains why the discrepancy between our expansion and numerics is largest at $R = 50$ and diminishes as R is increased to 100 and 500 (see Fig. 3b). However, even at $R = 50$, the asymptotic error is tolerable. Since the size of the boundary layer becomes considerably smaller at higher injection Reynolds numbers, its influence on the solution becomes less important as R is increased from moderate to large. The fact that the largest error is seen at the core does suggest the presence of a small boundary layer in that neighbourhood. Nonetheless, since this article focuses on the moderate-to-large injection driven flow, the small exponential corrections in the injection case will be considered too small in magnitude to justify their addition.

6.3 Axial velocity for constant crossflow reynolds numbers

In order to study the field sensitivity to α, the crossflow Reynolds number is now held constant at $R = 50$ and $R = -50$ in Figs. 4a and 4b. As α is varied from -10 to $+10$, both numerical and asymptotic solutions are compared. It thus becomes apparent that, for the same absolute value of the crossflow Reynolds number, the suction-flow approximation is more accurate and less sensitive to variations in α. Even so, the more accurate suction formulation (in Fig. 2b) corresponds to a negative α (i.e., contraction combined with suction). On the other hand, the injection solution becomes less accurate at higher values of α (i.e., as $|\alpha|$ approaches $|R|$). Furthermore, for the same absolute value of α, the injection solution becomes more accurate for positive α (i.e., expansion combined with injection).

6.4 Improved convergence in the suction flow approximation

As illustrated in the graphs above, it appears that the suction flow approximation is more accurate than the injection flow solution for the same level of suction or injection. In fact, using the favourable combination of injection $R = 100$ and expansion $\alpha = 10$, numerics and asymptotics can be compared in Table 1 with the less favourable combination of suction $R = -100$ and $\alpha = 10$. Despite the more favourable wall motion in the injection-expansion case, tabulated values indicate that a better agreement can

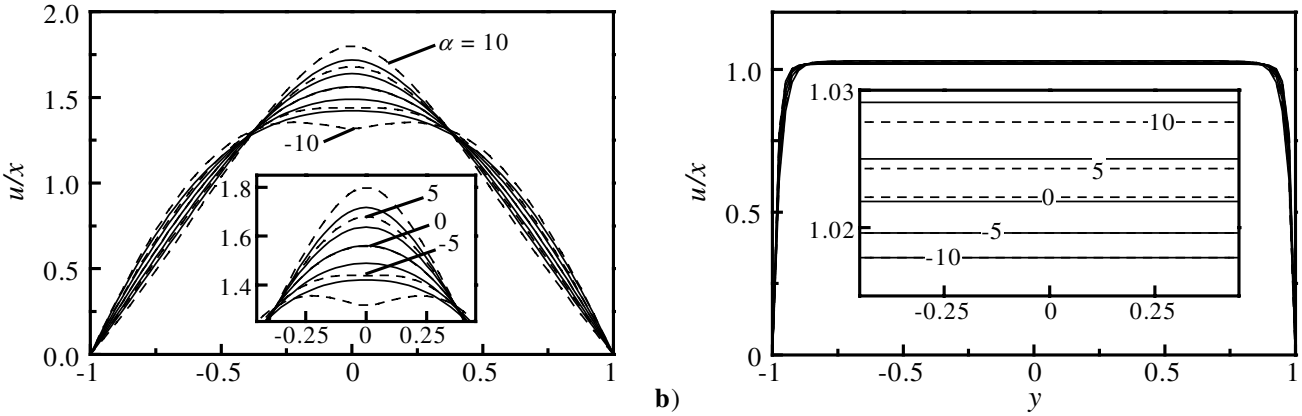

Fig. 4 Comparison between normalized axial velocities obtained from numeric (—) and asymptotic (- - -) solutions over a range of wall regression rates ($-10 \leq \alpha \leq 10$). The crossflow Reynolds numbers are a) 50 and b) -50.

Table 1 Comparison between numeric and asymptotic predictions for F at $\alpha = 10$, $R = 100$ and $R = -100$.

F	Injection $R = 100$		Suction $R = -100$	
y	numeric	eq. (62)	numeric	eq. (77)
0.0	0.00000	0.00000	0.00000	0.00000
0.1	0.16377	0.16414	0.10117	0.10116
0.2	0.32193	0.32254	0.20234	0.20232
0.3	0.46995	0.47078	0.30351	0.30349
0.4	0.60424	0.60523	0.40468	0.40465
0.5	0.72190	0.72292	0.50585	0.50581
0.6	0.82063	0.82154	0.60702	0.60697
0.7	0.89871	0.89938	0.70819	0.70813
0.8	0.95498	0.95535	0.80937	0.80930
0.9	0.98878	0.98890	0.91053	0.91045
1.0	1.00000	1.00000	1.00000	1.00000

be realized in the suction case. While the precision of the latter extends to 3 significant figures, the injection solution remains limited to 2 digits or less.

6.5 Limitations

Despite the improved accuracy of the suction formulation, it is clear that both asymptotic solutions deteriorate when the expansion or contraction ratios become of the same order as that of the crossflow Reynolds number. The only exception is that of increasing the contraction rate in the suction case. These observations can be explained by first considering the coefficient of the second term in eq. (34). By recalling that the relevant perturbation solution is based on the condition that $\alpha\varepsilon \ll 1$, it follows that, as α approaches R, the injection formulation becomes less reliable. For suction, on the other hand, since the effective perturbation parameter is based on the reciprocal of M, the expansion can also break down when the sum $\alpha + R$ is no longer large. This will be the case, for instance, when the expansion ratio $\alpha \to -R$ becomes a large positive number.

6.6 Flow streamlines

In order to help visualization of the fundamental flow structure, streamlines originating from several discrete locations along the wall are shown in Fig. 5 for several values of R and α. In Fig. 5a, increasing the Reynolds number from 50 to 500 in the presence of wall expansion seems to have a small effect on flow turning severity. In both cases, the fluid enters the expanding channel almost perpendicularly to the walls. When the flow direction is reversed, a smaller flow suction angle is induced at the wall. By comparison to the gradual turning of the injection-induced flow, the more sudden flow turning associated with the suction case leads to steeper velocity and therefore stress gradients near the wall. When the same comparison is repeated in Fig. 5b with a contraction of $\alpha = -10$, a more severe flow turning pattern is generally observed in both suction and moderate injection cases. The reason is this. As mass is injected more rapidly into the collapsing channel, removal of added mass near the head end requires an increasingly larger axial velocity component. Hence, in order to produce the necessary downstream convection, the relative magnitude of the axial versus normal velocity must increase with faster contraction rates. As explained earlier, for the large injection case (of $R = 500$), the solution becomes much less sensitive to α. On that account, no appreciable flow turning difference can be noted between Fig. 5a and 5b.

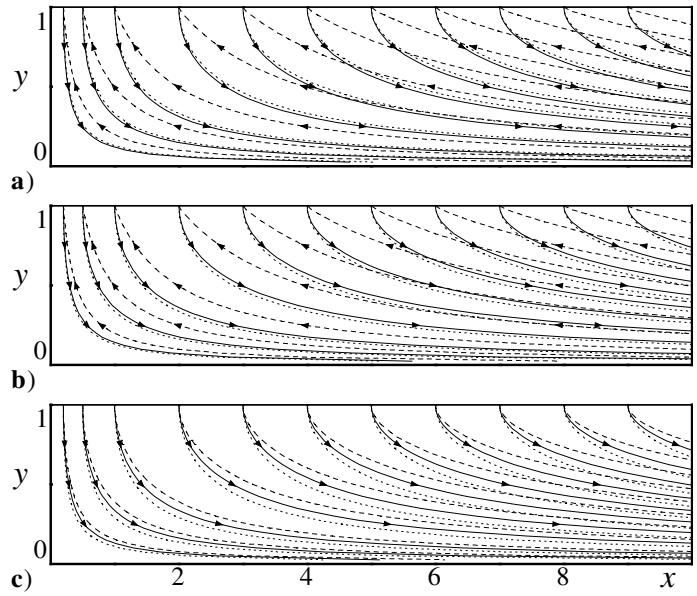

Fig. 5 Mean-flow streamlines for a) $\alpha = 10$ and b) $\alpha = -10$; $R = 50$ (—), -100 (- - -), and 500 ($\cdots$). In c), $R = 50$ and $\alpha = 0$ (—), -20 (- - -), and 20 ($\cdots$).

The effect of contracting or expanding walls is more clearly isolated in Fig. 5c where α is varied at constant R. By comparison with the $\alpha = 0$ motionless case, a steeper flow turning takes place when the channel walls are in the collapsing mode. This is accompanied by an increase in the relative magnitude of the axial to normal velocity ratio. Conversely, a more gradual flow turning occurs when the walls are in the expansion mode. The consistent reduction in the axial to normal velocity ratio with successive increases in α leads to an interesting hypothetical case. When that ratio reaches zero (for a sufficiently rapid wall regression), the expansion of the walls will exactly negate the effect of flow injection. In that event, the streamlines will remain perpendicular to the wall with a zero axial flow component.

7 The stress and pressure fields

The constant companions of the velocity field are now considered. These include the shear stress and pressure distributions in both axial and normal directions.

7.1 Shear stress distribution

To determine the shear stress, one may begin by considering Newton's law for viscosity, viz.

$$\bar{\tau} = \mu \left(\partial \overline{v} / \partial \overline{x} + \partial \overline{u} / \partial \overline{y} \right). \tag{81}$$

Inserting the velocity into eq. (81) renders

$$\bar{\tau} = \rho \nu^2 \bar{x} a^{-3} \bar{F}_{yy}. \tag{82}$$

The shear stress may be made dimensionless by using the dynamic pressure as a reference. At the outset, one gets

$$\tau = \bar{\tau} / (\rho v_{\mathrm{w}}^2) = \varepsilon x F_{yy}. \tag{83}$$

This simple formulation leads to a useful expression for the stress at the wall, namely, to $\tau_{\mathrm{w}} = \varepsilon x F_{yy}\,(1)$. Consequent numerical and asymptotic predictions can be compared in Fig. 6. Aside from the fair agreement between numerics and asymptotics, one may note a significant shear stress increase in the wall suction case. This increase becomes even more pronounced in Fig. 6b when the walls are in contraction. The increased τ_{w} for suction flows is consistent with the velocity field description and may be attributed to the increased flow turning severity and steeper velocity gradients near the wall. For injection, the shear stress is negative due to the reversal in axial flow direction. The stress also decreases at higher Reynolds numbers since, as R becomes larger, the role of viscosity diminishes, the shear at the wall becomes less appreciable, and the viscous layer becomes thinner and further distanced from the wall (cf. Proudman [7]). Here too, the agreement between asymptotics and numerics improves at larger values of R.

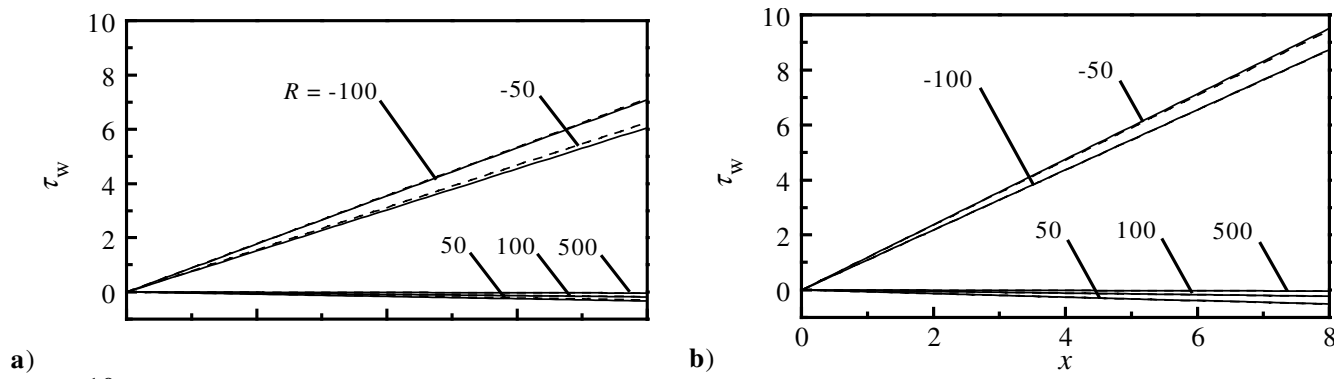

Fig. 6 Comparison between numeric (—) and asymptotic (- - -) wall shear stresses for a) $\alpha = 10$ and b) $\alpha = -10$; $-100 \leq R \leq 500$.

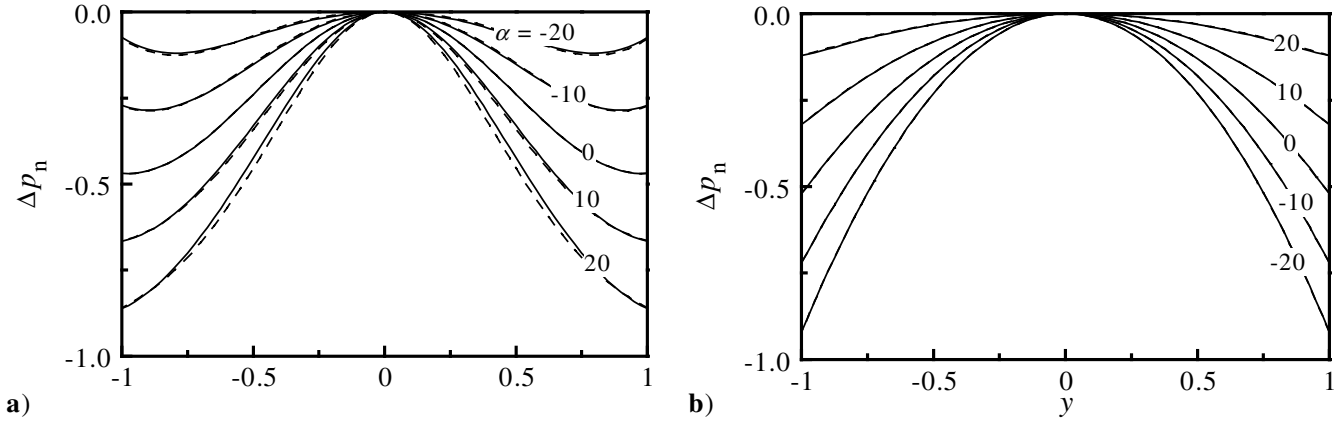

Fig. 7 Comparison between numeric (—) and asymptotic (- - -) pressure drops in the normal direction for a) $R = 50$ and b) $R = -50$; $-20 \leq \alpha \leq 20$.

7.2 Normal pressure drop

In order to determine the normal pressure drop, one can begin by substituting eq. (15) into eq. (3). Since $y = y(t)$, derivatives must be carefully manipulated. To proceed, one first evaluates

$$\frac{\partial \bar{v}}{\partial t} = \frac{\nu^2 \alpha}{a^3}\left(\bar{F} + y\bar{F}_y\right), \quad \frac{\partial \bar{v}}{\partial \bar{x}} = 0, \quad \frac{\partial^2 \bar{v}}{\partial \bar{x}^2} = 0, \quad \bar{v}\frac{\partial \bar{v}}{\partial \bar{y}} = \frac{\nu^2}{a^3}\bar{F}\bar{F}_y, \quad \frac{\partial^2 \bar{v}}{\partial \bar{y}^2} = -\frac{\nu}{a^3}\bar{F}_{yy}. \tag{84}$$

Following substitution into eq. (3), a simple rearrangement yields

$$p_y = -\left[\varepsilon F_{yy} + FF_y + \alpha\varepsilon\left(F + yF_y\right)\right]; \quad p \equiv \bar{p}/\rho v_w^2. \tag{85}$$

The normal pressure distribution can now be determined by integrating eq. (85) with the boundary conditions given by eq. (33). Letting p_c be the centreline pressure, one may start with

$$\int_{p_c}^{p(y)} \mathrm{d}p = \int_0^y -\left[\varepsilon F_{yy} + FF_y + \alpha\varepsilon\left(F + yF_y\right)\right] \mathrm{d}y. \tag{86}$$

Recognizing that $FF_y = \frac{1}{2}(F^2)_y$, and $(F + yF_y) = (yF)_y$, one may substitute these relations into eq. (86). Subsequent integration yields

$$\Delta p_n \equiv p(y) - p_c = \varepsilon F_y(0) - \left(\varepsilon F_y + \tfrac{1}{2}F^2 + \alpha\varepsilon yF\right). \tag{87}$$

Figs. 7a and 7b illustrate the pressure drop for $R = 50$ and $R = -50$. As α is varied from -20 to $+20$, one may note that the pressure drop increases with α for injection (Fig. 7a), but decreases for suction (Fig. 7b). One may also note that, except for injection combined with wall contraction, the absolute pressure drop is largest near the walls. For $R = 50$ and negative α, the maximum (absolute) pressure drop occurs somewhere between the midsection plane and the wall. Overall, the asymptotic approximation appears to hold quite well up to $|\alpha| = 20$, a value that is of the same order as R. One also notes that, for injection and small $\varepsilon\alpha$ in Fig. 7a, the pressure gradient p_y is near zero at the wall. This is consistent with the behaviour of Taylor's ideal profile [2].

7.3 Axial pressure drop

Using

$$\bar{u}_t = \frac{\nu \bar{x}}{a^2} \bar{F}_{yy} \frac{\partial y}{\partial t} - \frac{2\nu \bar{x} \dot{a}}{a^3} \bar{F}_y, \tag{88}$$

substitution into eq. (2) leads to the axial pressure gradient. One finds

$$p_x = x \left[\varepsilon F_{yyy} + F F_{yy} + (F_y)^2 \ + \alpha\varepsilon \left(2F_y + y F_{yy} \right) \right]. \tag{89}$$

Subsequent integration gives the axial pressure distribution at any streamwise location, namely,

$$\Delta p_{\mathrm{a}} = \tfrac{1}{2} x^2 \left[\varepsilon F_{yyy} + F F_{yy} + (F_y)^2 \ + \alpha\varepsilon \left(2F_y + y F_{yy} \right) \right]. \tag{90}$$

One finds Δp_{a} to vary slowly in the axial direction. The agreement between asymptotics and numerics is also improved with $|R|$.

8 Conclusions

In this article, an exact similarity solution for the Navier-Stokes equations is presented. The problem arises in the context of a fluid entering a porous channel with moving walls. The similarity transformations in space and time convert the momentum equation into a single, nonlinear, differential equation. It can be easily verified that the resulting equation reduces to the classic Berman equation for a channel with stationary walls. Closed-form solutions obtained using regular perturbations and the method of variation of parameters are shown to coincide with the numerical solution over a useful range of parameters. Due to their adequate accuracy, the explicit formulations presented here are practically equivalent to the exact solution over a range of moderate-to-high Reynolds numbers. When injection is increased, the effect of varying the expansion rate becomes less pronounced. Larger values of R/α and $(R + \alpha)$ improve the accuracy of the asymptotic approximations in injection and suction-induced flows, respectively. Their improved accuracy makes them suitable for modelling the hard-blowing or hard-suction phenomena in deformable channels.

For injection-induced flows, increasing the Reynolds number is also found to accelerate flow turning and to increase the ratio of axial to normal velocities. Conversely, increasing wall expansion seems to inhibit flow turning and decrease the shear stress at the wall. For injection Reynolds numbers in excess of 500, our viscous solution approaches Taylor's inviscid sinusoidal profile provided that the expansion rate remains reasonably small. Similarly, for suction Reynolds numbers below -50, our asymptotic approximation approaches Sellars' linear profile. As such, our formulations embrace former solutions presented by Taylor [2], Yuan [3], and Terrill [4] for injection, and by Sellars [5] and Terrill [6] for suction in nonexpanding channels. The refinement associated with the current generalization enables us to better model transpiration cooling and the hard-blowing mechanism in cold-flow simulations of slab rocket motors. When fed into the aeroacoustic solution for rocket chambers [36], a fully rotational and viscous field is now made possible. When wall expansions are periodically followed by contractions, the resulting motion can be used to mimic the peristaltic motion of slit flows confined between parallel membranes. This motion can be useful in modelling physiological processes involving flow filtration and seepage.

Acknowledgements The authors wish to thank NASA and the Wisconsin Space Grant Consortium for their partial support of this work.

References

[1] A. S. Berman, Laminar flow in channels with porous walls, J. Appl. Phys. **24**, 1232–1235 (1953).
[2] G. I. Taylor, Fluid flow in regions bounded by porous surfaces, Proc. R. Soc. Lond. A **234**, 456–475 (1956).
[3] S. W. Yuan, Further investigation of laminar flow in channels with porous walls, J. Appl. Phys. **27**, 267–269 (1956).
[4] R. M. Terrill, Laminar flow in a uniformly porous channel with large injection, Aeronaut. Q. **16**, 323–332 (1965).
[5] J. R. Sellars, Laminar flow in channels with porous walls at high suction Reynolds numbers, J. Appl. Phys. **26**, 489–490 (1955).
[6] R. M. Terrill, Laminar flow in a uniformly porous channel, Aeronaut. Q. **15**, 299–310 (1964).
[7] I. Proudman, An example of steady laminar flow at large Reynolds number, J. Fluid Mech. **9**, 593–612 (1960).
[8] G. M. Shrestha and R. M. Terrill, Laminar flow with large injection through parallel and uniformly porous walls of different permeability, Quart. J. Mech. Appl. Math. **21** , 413–432 (1968).
[9] M. Morduchow, On laminar flow through a channel or tube with injection: application of method of averages, Quart. J. Appl. Math. **14**, 361–368 (1957).
[10] F. M. White jr., B. F. Barfield, and M. J. Goglia, Laminar flow in a uniformly porous channel, Trans. ASME: J. Appl. Mech. E **25**, 613–617 (1958).
[11] R. M. Terrill and G. M. Shrestha, Laminar flow through parallel and uniformly porous walls of different permeability, Z. Angew. Math. Phys. **16**, 470–482 (1965).
[12] S. M. Cox, Two-dimensional flow of a viscous fluid in a channel with porous walls, J. Fluid Mech. **227** 1–33 (1991).

[13] J. R. King and S. M. Cox, Asymptotic analysis of the steady-state and time-dependent Berman problem, J. Eng. Math. **39**, 87–130 (2001).
[14] M. B. Zaturska, P. G. Drazin, and W. H. H. Banks, On the flow of a viscous fluid driven along a channel by suction at porous walls, Fluid Dyn. Res. **4**, 151–178 (1988).
[15] C. L. Taylor, W. H. H. Banks, M. B. Zaturska, and P. G. Drazin, Three-dimensional flow in a porous channel, Quart. J. Mech. Appl. Math. **44**, 105–133 (1991).
[16] E. B. B. Watson, W. H. H. Banks, M. B. Zaturska, and P. G. Drazin, On transition to chaos in two-dimensional channel flow symmetrically driven by accelerating walls, J. Fluid Mech. **212**, 451–485 (1990).
[17] P. Watson, W. H. H. Banks, M. B. Zaturska, and P. G. Drazin, Laminar channel flow driven by accelerating walls, Europ. J. Appl. Math. **2**, 359–385 (1991).
[18] S. M. Cox and A. C. King, On the asymptotic solution of a high-order nonlinear ordinary differential equation, Proc. R. Soc. Lond. A **453**, 711–728 (1997).
[19] A. D. MacGillivray and C. Lu, Asymptotic solution of a laminar flow in a porous channel with large suction: a nonlinear turning point problem, Meth. Appl. Anal. **1**, 229–248 (1994).
[20] C. Lu, On the asymptotic solution of laminar channel flow with large suction, SIAM J. Math. Anal. **28** , 1113–1134 (1997).
[21] V. N. Varapaev and V. I. Yagodkin, Flow stability in a channel with porous walls, Fluid Dyn. (Izv. AN SSSR. MZhG) **4**, 91–95 (1969).
[22] G. D. Raithby, and D. C. Knudsen, Hydrodynamic development in a duct with suction and blowing, Trans. ASME: J. Appl. Mech. E **41**, 896–902 (1974).
[23] L. M. Hocking, Non-linear instability of the asymptotic suction velocity profile, Quart. J. Mech. Appl. Math. **28**, 341–353 (1975).
[24] A. A. Sviridenkov and V. I. Yagodkin, Flow in the initial sections of channels with permeable walls, Fluid Dyn. (Izv. AN SSSR. MZhG) **11**, 689–693 (1976).
[25] J. F. Brady, Flow development in a porous channel or tube, Phys. Fluids **27**, 1061–1067 (1984).
[26] L. Durlofsky and J. F. Brady, The spatial stability of a class of similarity solutions, Phys. Fluids **27**, 1068–1076 (1984).
[27] W. A. Robinson, The existence of multiple solutions for the laminar flow in a uniformly porous channel with suction at both walls, J. Eng. Math. **10**, 23–40 (1976).
[28] F. M. Skalak and C.-Y. Wang, On the nonunique solutions of laminar flow through a porous tube or channel, SIAM J. Appl. Math. **34**, 535–544 (1978).
[29] K.-G. Shih, On the existence of solutions of an equation arising in the theory of laminar flow in a uniformly porous channel with injection, SIAM J. Appl. Math. **47**, 526–533 (1987).
[30] S. P. Hastings, C. Lu, and A. D. MacGillivray, A boundary value problem with multiple solutions from the theory of laminar flow, SIAM J. Math. Anal. **23** , 201–208 (1992).
[31] C. Lu, A. D. MacGillivray, and S. P. Hastings, Asymptotic behaviour of solutions of a similarity equation for laminar flows in channels with porous walls, IMA J. Appl. Math. **49**, 139–162 (1992).
[32] S. Apte and V. Yang Effect of acoustic oscillation on flow development in a simulated nozzleless rocket motor. In: Solid Propellant Chemistry, Combustion, and Motor Interior Ballistics, edited by V. Yang, T. B. Brill, and W.-Z. Ren, Washington, DC, 2000, pp. 791–822.
[33] Y. Lee and R. A. Beddini, Acoustically-induced turbulent transition in solid propellant rocket chamber flowfields, AIAA Paper 99-2508, 1999.
[34] Lee, Y. and R. A. Beddini: Effect of solid rocket chamber pressure on acoustically-induced turbulent transition, AIAA Paper 2000-3802, 2000.
[35] G. A. Flandro and J. Majdalani, Aeroacoustic instability in rockets, AIAA Paper 2001-3868, 2001.
[36] J. Majdalani and T. S. Roh, The oscillatory channel flow with large wall injection, Proc. Roy. Soc. A **456** 1625–1657 (2000).
[37] T. L. Jackson, J. Buckmaster, M. Campbell, S. Kochevets, and L. Massa: The burning of 3D random-pack heterogeneous propellants, AIAA Paper 2001-3952, 2001.
[38] J. Buckmaster, T. L. Jackson, and M. Ulrich, Numerical modeling of heterogeneous propellant combustion, AIAA Paper 2001-3579, 2001.
[39] S. Tsangaris and E. Leiter, On laminar steady flow in sinusoidal channels, J. Eng. Math. **18**, 89–103 (1984).
[40] J. Barron, J. Majdalani, and W. K. Van Moorhem, A novel investigation of the oscillatory field over a transpiring surface, J. Sound Vib. **235** , 281–297 (2000).
[41] Y. Ma, W. K. Van Moorhem, and R. W. Shorthill, Experimental investigation of velocity coupling in combustion instability, J. Propul. Power **7**, 692–699 (1991).
[42] Y. Ma, W. K. Van Moorhem, and R. W. Shorthill, Innovative method of investigating the role of turbulence in the velocity coupling phenomenon, ASME J. Vibr. Acoust. **112**, 550–555 (1990).
[43] J. C. Traineau, P. Hervat, and P. Kuentzmann, Cold-flow simulation of a two-dimensional nozzleless solid-rocket motor, AIAA Paper 86-1447, 1986.
[44] G. Avalon, G. Casalis, and J. Griffond, Flow instabilities and acoustic resonance of channels with wall injection, AIAA Paper 98-3218, 1998.
[45] G. Casalis, G. Avalon, and J.-P. Pineau, Spatial instability of planar channel flow with fluid injection through porous walls, Phys. Fluids **10**, 2558–2568 (1998).
[46] J. Griffond and G. Casalis, On the dependence on the formulation of some nonparallel stability approaches applied to the Taylor flow, Phys. Fluids **12**, 466–468 (2000).
[47] J. Griffond and G. Casalis, On the nonparallel stability of the injection induced two-dimensional Taylor flow, Phys. Fluids **13**, 1635–1644 (2001).,
[48] S. Apte and V. Yang, Effects of acoustic oscillations on turbulent flowfield in a porous chamber with surface transpiration, AIAA Paper 98-3219, 1998.
[49] T.-M. Liou and W.-Y. Lien, Numerical simulations of injection-driven flows in a two-dimensional nozzleless solid-rocket motor, J. Propul. Power **11**, 600–606 (1995).
[50] T. M. Liou, W. Y. Lien, and P. W. Hwang, Transition characteristics of flowfield in a simulated solid-rocket motor, J. Propul. Power **14**, 282–289 (1998).

[51] S. Uchida and H. Aoki, Unsteady flows in a semi-infinite contracting or expanding pipe, J. Fluid Mech. **82**, 371–387 (1977).
[52] M. Goto and S. Uchida, Unsteady flows in a semi-infinite expanding pipe with injection through wall, Trans. Japan Soc. Aeronaut. Space Sci. **33**, 14–27 (1990).
[53] A. A. Kozinski, F. P. Schmidt, and E. N. Lightfoot, Velocity profiles in a porous-walled duct, Ind. Eng. Chem. Fund. **9**, 502–505 (1970).
[54] C. Y. Wang, Pulsatile flow in a porous channel, Trans. ASME: J. Appl. Mech. **38**, 553–555 (1971).
[55] R. K. Bhatnager, Fluctuating flow of a viscoelastic fluid in a porous channel, Trans. ASME: J. Appl. Mech. **46**, 21–25 (1979).
[56] R. M. Terrill, On some exponentially small terms arising in flow through a porous pipe, Quart. J. Mech. Appl. Math. **26**, 347–354 (1973).